Oxygen Vacancies Engineering in Thick Semiconductor Films via Deep Ultraviolet Photoactivation for Selective and Sensitive Gas Sensing

Zain Ul Abideen, Jun-Gyu Choi, Jodie A. Yuwono, Alexander Kiy, Priyank Vijaya Kumar, Krishnan Murugappan, Won-June Lee, Patrick Kluth, David R. Nisbet, Thanh Tran-Phu, Myung-Han Yoon,* and Antonio Tricoli*

Room-temperature detection of volatile organic compounds in particle-per-billion concentrations is critical for the development of wearable and distributed sensor networks. However, sensitivity and selectivity are limited at low operating temperatures. Here, a strategy is proposed to substantially improve the performance of semiconductor sensors. Tunable oxygen vacancies in thick 3D networks of metal oxide nanoparticles are engineered using deep ultraviolet photoactivation. High selectivity and sensitivity are achieved by optimizing the electronic structure and surface activity while preserving the 3D morphology. Cross-sectional depth analysis reveals oxygen vacancies present at various depths ($\approx$24% at a depth of 1.13 µm), with a uniform distribution throughout the thick films. This results in $\approx$58% increase in the sensitivity of ZnO to 20-ppb ethanol at room temperature while $\approx$51% and 64% decrease in the response and recovery times, respectively. At an operating temperature of 150 °C, oxygen-vacant nanostructures achieve a lower limit of detection of 2 ppb. Density functional theory analysis shows that inducing oxygen vacancies reduces activation energy for ethanol adsorption and dissociation, leading to improved sensing performance. This scalable approach has the potential for designing low-power wearable chemical and bio-sensors and tuning the activity and band structure of porous, thick oxide films for multiple applications.

1. Introduction

The development of portable and wearable chemical and biosensors is increasingly important for point-of-care and self-monitoring medical devices. Furthermore, increasing industrialization is resulting in severe air pollution.[1] These pollutants consist of toxic particulates, gas molecules, and volatile organic compounds (VOCs) such as ethanol, benzene, toluene, and formaldehyde.[2] Continuous monitoring of these pollutants and VOCs at low concentrations with room-temperature and low-power consumption devices is important to maintain a safe and sustainable environment. Among several types of sensing technologies, metal oxide semiconductor (MOS)-based chemiresistive sensors have been extensively studied, due to their sensitivity to a variety of gaseous analytes, low cost, and ease of miniaturization as well as the potential for integration in sensor arrays.[3]

Z. U. Abideen, K. Murugappan, T. Tran-Phu, A. Tricoli
Nanotechnology Research Laboratory
Research School of Chemistry
College of Science
Australian National University
Canberra, ACT 2601, Australia
E-mail: antonio.tricoli@sydney.edu.au

J.-G. Choi, W.-J. Lee, M.-H. Yoon
School of Materials Science and Engineering
Gwangju Institute of Science and Technology (GIST)
Gwangju 61005, Republic of Korea
E-mail: mhyoon@gist.ac.kr

J. A. Yuwono, P. V. Kumar
School of Chemical Engineering
University of New South Wales (UNSW)
Sydney 2052, Australia

J. A. Yuwono
College of Engineering, Computing and Cybernetics
Australian National University
Canberra, ACT 2601, Australia

J. A. Yuwono
School of Chemical Engineering
The University of Adelaide
Adelaide 5000, Australia

A. Kiy, P. Kluth
Department of Materials Physics
Research School of Physics
Australian National University
Canberra, ACT 2601, Australia

K. Murugappan
CSIRO
Mineral Resources
Private Bag 10, Clayton South, Victoria 3169, Australia

**ADVANCED
SCIENCE NEWS**
www.advancedsciencenews.com

**ADVANCED
ELECTRONIC
MATERIALS**
www.advelectronicmat.de

MOS sensors and chemiresistive sensing technology have the potential for low-powered portable devices, due to their promising electrical properties and chemical stability. However, some major drawbacks of this sensing technology are its poor selectivity, especially in sub-ppm concentrations. Moreover, such sensors usually suffer from long response and recovery times at low operating temperatures.[4] For instance, low concentrations (1 to 2 ppm) of breath acetone represent a basal level of ketosis and have been used as a metabolic biomarker in healthy people.[5] Similarly, the concentrations of acetone and ethanol in the breath of lung cancer patients are 44–2744 and 64–2160 ppb, respectively. Therefore, the detection limit of a sensor must reach a few ppb for medical and other applications.[6] Moreover, MOS sensors generally perform best at higher temperatures such as 200–450 °C, which increases the complexity of the device, increases power consumption, and may reduce the long-term stability of the sensing layer.[7]

Various strategies are being explored to overcome these drawbacks such as the use of nanostructures with increased surface area, engineering the composition of the sensing layer by doping or creating defects,[8] tailoring the conditions of the sensing environment by using external illumination/irradiation and catalysts to improve the catalytic activity of the sensing environment.[4a,9] However, despite significant advancements in sensor technology, poor selectivity for extremely low concentration (<ppm) at room temperature as well as relatively high-power consumption are still major obstacles in the deployment of chemiresistive sensors for mobile and portable applications.[10]

A variety of MOS such as ZnO,[11] SnO$_2$,[12] TiO$_2$,[13] WO$_3$,[14] In$_2$O$_3$,[15] and NiO[9b] have been investigated for low-temperature VOCs sensing. Nanostructures with high specific surface area and large surface-to-volume ratios such as core–shell,[16] nanobelts,[17] nanorods[18] have demonstrated their potential for room temperature VOCs detection. The composition of these structures has been engineered to increase their room temperature sensitivity and lower the limit of detection by using dopants and by creating and tuning defects in the nanostructures.[9b,19] More recently, oxygen defect engineering has been proposed to improve the catalytic and sensing performances of metal oxides by modulating the electronic structure of the material.[20] In general, oxygen vacancies improve the sensitivity of a sensor by changing the electron density of the sensor material, which in turn improves the adsorption of target gas molecules and the electrical conductivity of the nanostructures by lowering the conduction band.

As a well-known derivative for producing oxygen vacancies, external light illumination during device operation has been a promising candidate to promote surface photocatalytic reactions, which both increases the catalytic activity and facilitates rapid detection of VOCs at room temperature.[4a,9b] Recently, enhancement in the sensitivity and selectivity of mesoporous ZnO nanosheets at room temperature was achieved for methane gas molecule sensing by creating surface oxygen vacancies and using external UV-activation of the nanosheets.[21] However, the limit of detection of the device was high (1000 ppm), making it impractical for breath analysis, where the concentration of VOCs is often in the ppb range. Similarly, SnO$_2$ nanostructured thin films have been reported for room temperature VOCs sensing, where oxygen defects played a significant role in room temperature gas sensing. However, the lower limit of detection was 25 ppm and the efficacy of light illumination for activating photocatalytic reactions was limited to the surface of thin SnO$_2$ films. Importantly, there was no change in oxygen vacancies inside the films despite having a high surface-to-volume ratio.[22]

More recently, the gas sensing performance of ZnO nanosheets in which oxygen vacancies were derived from metal–organic frameworks has been investigated. The sensors were able to detect the trace concentration (20 ppb) of CO gas, however, this lower limit of detection (20 ppb) was achieved at 300 °C.[23] In our previous studies, fully electron depleted ZnO nanoparticles of sizes less than two times of Debye length were fabricated by hot-aerosol synthesis, which provides the benefit of high porosity, purity, and controllable particle size.[24] As such, various MOS porous films synthesized by the aerosol method have been investigated for the detection of trace concentrations of VOCs.[9b,24a] In parallel, it has been reported that the photoactivation by deep ultraviolet (DUV) at a relatively low temperature could increase the contents of oxygen vacancies by inducing oxygen vacancies in semiconductor films and further increase the surface-to-volume ratio of the nanostructures.[25]

Here, we build on these previous findings and propose a method to synthesize thick, ultraporous networks of MOS nanoparticles with tunable oxygen vacancies for low-temperature detection of VOCs with high sensitivity and selectivity. Micrometer-thick layers of ultraporous, fully electron depleted, ZnO nanoparticle networks were fabricated via hot-aerosol synthesis. Oxygen vacancies were introduced in these 3D networks by DUV

D. R. Nisbet
The Graeme Clark Institute
The University of Melbourne
Melbourne 3010, Australia

D. R. Nisbet
Laboratory of Advanced Biomaterials
Research School of Chemistry and the John Curtin School
of Medical Research
the Australian National University
Canberra, ACT 2601, Australia

D. R. Nisbet
Department of Biomedical Engineering
Faculty of Engineering and Information Technology
The University of Melbourne
Melbourne 3010, Australia

D. R. Nisbet
Melbourne Medical School
Faculty of Medicine
Dentistry and Health Science
The University of Melbourne
Melbourne 3010, Australia

A. Tricoli
Nanotechnology Research Laboratory
Faculty of Engineering
University of Sydney
Sydney, NSW 2006, Australia

photoactivation at 200 °C, leading to a unique morphology consisting of thick and highly porous 3D networks of oxygen-vacant nanoparticles. These structural characteristics enabled the presence of oxygen vacancies at the surface, and for the first time, several micrometers below the surface of the semiconductor film. The presence of oxygen vacancies in the entire 3D nanoparticle network, coupled with its high porosity facilitated the reversible diffusion and reaction of VOC molecules. This enhanced the sensitivity of the films to ppb concentrations at room temperature, whilst also lowering the limit of detection to 2 ppb at an optimal operating temperature of 150 °C. Density functional theory (DFT) calculations were performed to elucidate the sensing mechanism and ethanol interaction with the sensing layer. The superior sensing performance was attributed to the synergistic effects of photoinduced ions, unpaired electrons, high concentration of oxygen vacancies throughout the 3D networks, high porosity,

and increased specific surface area. This approach provides a tool to engineer highly performing MOS films with tunable oxygen vacancies, high and accessible surfaces with applications ranging from gas sensing to (photo)catalysis and photodetection.

2. Results and Discussion

A schematic illustration of the flame spray pyrolysis (FSP) used to synthesize ultraporous ZnO nanoparticle networks and the DUV photoactivation step for oxygen vacancy engineering is shown in **Figure 1**. ZnO nanoparticle networks were self-assembled on interdigitated Pt electrodes by thermophoretic deposition of flame-made ZnO aerosols. The thickness of the deposited films was linearly dependent on the deposition time. A thickness of ≈6 μm was selected in line with previous
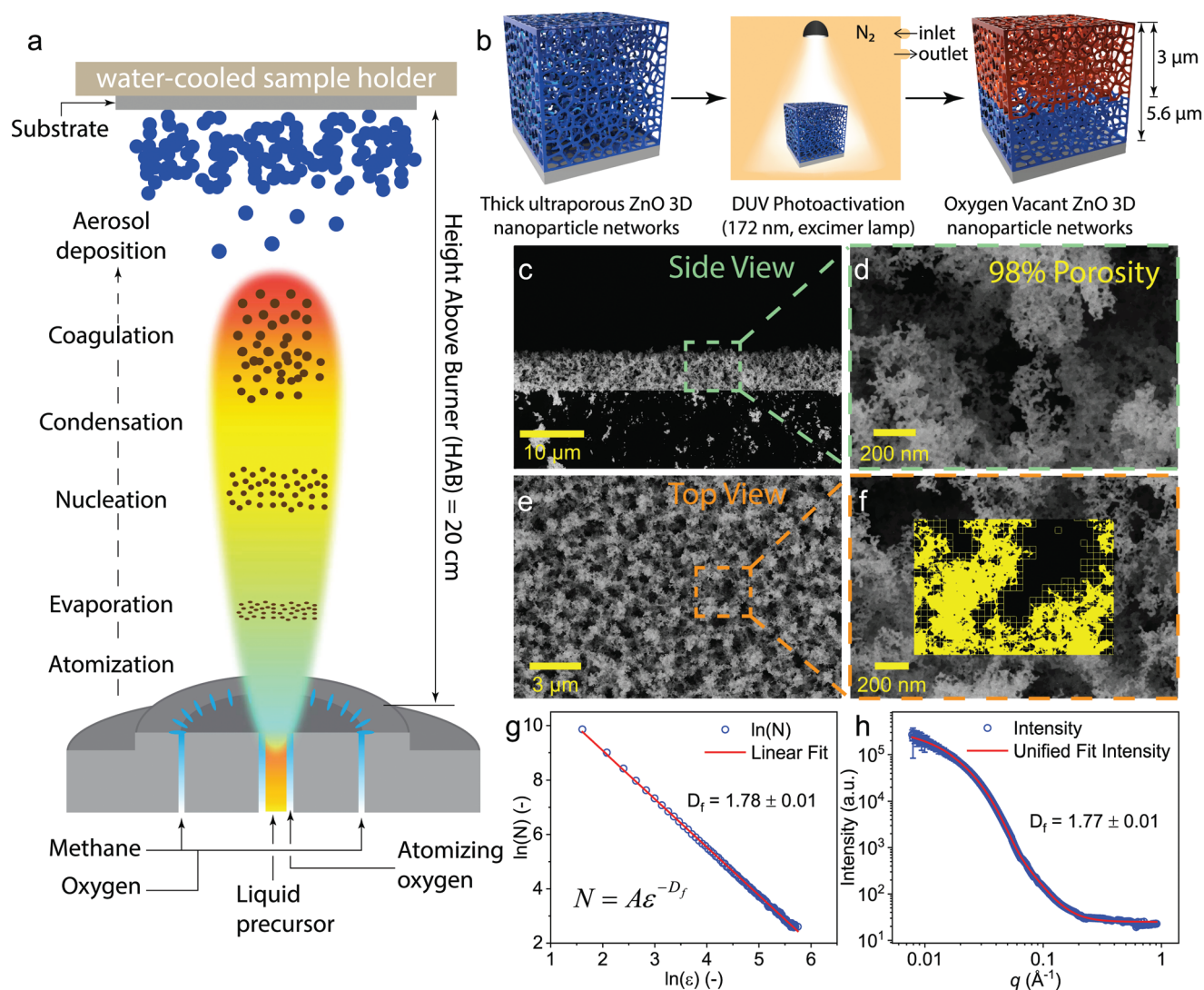

Figure 1. a) Schematic illustration of the FSP process for the deposition of thick ultraporous ZnO films. b) DUV photoactivation illustration for thick ultraporous ZnO nanostructures. c–f) SEM images of ZnO at different magnifications for (c,d) cross-sectional view and (e,f) top-view with the inset in (f) showing the fractal generated image. (c) Cross-sectional SEM image showing uniform thickness of ≈6 μm ZnO film. (d) High-resolution cross-sectional SEM image of ZnO fractals. (e) Top-view of ZnO film. g,h) Fractal analysis (g) using the box-counting algorithm: double-log plot of foreground pixel number as a function of the scaling factor (h) small-angle X-ray scattering intensity as a function of wavenumber and respective fractal dimension (D_f).

literature on high-performance room temperature VOC sensors and UV photodetectors.[9b,24a] Subsequently, the films were sintered in air at a temperature of 300 °C for 12 h to remove potentially adsorbed contaminants. This was followed by DUV photoactivation at 200 °C using an excimer lamp (30 mW cm^{-2}) in a nitrogen atmosphere to generate vacancies in 3D ZnO nanostructures (see the Experimental Section). The short-wavelength (172 nm) high-energy (7.2 eV) DUV irradiation at low temperature under inert ambient conditions was suitable for deep penetration into the thick ultraporous networks via scattering and oxygen vacancy generation without absorption by ambient oxygen gas, while the 3D nanostructures remain intact (Figure 1b). The films were not scratch resistant, and a scratch could easily damage the film or the Pt electrodes beneath the film and on top of the substrate. However, without direct physical contact, the films were robust and were not damaged during transport and handling. The DUV-treated ZnO sensors are further referred to as oxygen vacant ZnO.

Figure 1c shows cross-sectional scanning electron microscopy (SEM) images of the films, which show neither visible cracks nor defects, in line with previous reports.[9b,24a,26] These films have ≈98% porosity (see the Experimental Section) and a bimodal hierarchical pore size distribution with large pores of 1–4 mm and small mesopores of a few tens of nanometers as shown in the high-resolution cross-sectional and top views of SEM images (Figure 1c–f). The high porosity and specific surface area of the films prepared by FSP provide a unique opportunity for efficient adsorption of target gas molecules, increasing the sensitivity of the devices.

Further top-view and cross-sectional SEM analysis of FSP-made ZnO layers (Figure S1, Supporting Information) reveal that the nanoparticle fractals are self-similar and self-repeatable. Flame-made nanostructures, which are controlled by stochastic self-assembly of nanoparticles, have fractal dimensions of 1.75 to 2.5, depending on the sintering level.[13b,27] Fractal structures are identified using scattering techniques such as light, X-ray, neutron scattering, or using image analysis.[28] We have previously demonstrated consistency between these methods to determine fractal dimensions (D_f) of flame-made films or powder.[26c,29] Here, the fractals were quantitatively analyzed by two key parameters: fractal dimensions and lacunarity via image processing analysis through box-counting algorithms.[28b] The SEM image used for this analysis and the fractal image generated by pixel distribution is shown in Figure 1f. The basic principle of this algorithm relies on laying the SEM image with a grid and the number of boxes with always decreasing dimensionality, which is required to cover the analyzed object, is counted. In this way, the structure of the pattern is captured with high accuracy. The fractal dimension, D_f, is a dimensionless number, which measures the degree of complexity of a system providing the likelihood that an object is invariant at different scales. It was evaluated by the following equation[13a,26c]

$$D_f = \lim_{\varepsilon \to 0} \frac{\log N}{\log \varepsilon} \tag{1}$$

where N is the number of boxes with edge ε needed to cover the object in each step. Figure 1f visualizes the fractal dimension of ZnO fractals as the slope of ln N versus ln ε plot, which results in a D_f of 1.78 ± 0.01.

To corroborate these findings, small-angle X-ray scattering (SAXS) measurements were carried out to analyze the fractal dimension and particle size of ZnO nanostructures (Figure 1h). The unified fitting of the SAXS data in the mass-fractal regime reveals a D_f value of 1.77 ± 0.01. This is in excellent agreement with the topological analysis, carried out using the box-counting algorithm, and is consistent with previous reports on the fractal dimension of hot-aerosol synthesized nanostructures.[20b,30]

An SAXS particle size (d_p) of 10.8 nm was fitted for the ZnO nanoparticle networks, which is in good agreement with the particle size estimated from transmission electron microscopic (transmission electron microscopy (TEM) and X-ray diffraction (XRD) analysis (see **Figure 2**c,e). The lacunarity, Λ, is correlated to the morphological inhomogeneity of fractal structures. It quantifies the heterogeneity or texture of the structure indicating how the fractal space is filled with gaps: the higher the lacunarity the lower the homogeneity.[31] Here, the mean Λ has been calculated from the variance, σ, and the mean, μ, of the foreground pixel distribution. The plot of the lacunarity versus the analyzed box length in Figure S1 of the Supporting Information shows the maximum is between 0 and 0.5 μm (0–500 nm), indicating that the highest level of inhomogeneity is in this length scale, upon which the film provides a degree of uniform disorder. This is as well a value for the radius of gyration.

TEM analysis of ZnO films reveals that the ZnO nanoparticles are quasi-spherical and are aggregated in large fractal structures (Figure 2a; Figure S2a, Supporting Information) with the inset in Figure 2a showing the diffraction pattern with simulated rings confirming high purity and high crystallinity of ZnO films (see the Experimental Section). The mean diameter of the particles, d_p, 10.97 ± 0.18 nm was calculated by the average of 625 nanoparticles analyzed by TEM images (Figure 2b). The high-resolution TEM (HRTEM) images confirm the crystalline features of ZnO with a lattice spacing of 2.81 Å, which is consistent with the (100) plane of ZnO (Figure 2c).[32]

XRD analysis was also carried out to further confirm the grain size and the crystallinity of the films. Figure 2d shows the typical XRD patterns of as-prepared and oxygen vacant ZnO porous films. All the peaks were well aligned with the reference pattern of ICSD 98-015-4489 (Inorganic Crystal Structure Database, ICSD). The crystal structure of ZnO is hexagonal with the space group of $P63mc$. The mean crystal size of 10.37 nm was calculated for the as-prepared ZnO films, while 10.91 nm was calculated for the oxygen vacant ZnO films using the modified Scherrer equation[33] from XRD data (see the Experimental Section). The latter average crystal sizes are in good agreement with the mean particle size of 10.97 nm calculated by TEM analysis (Figure 2b) and 10.8 nm by SAXS analysis, indicating mainly monocrystalline nanoparticles.

Together with the XRD, SEM, and TEM analysis, it was concluded that crystalline and ultraporous ZnO nanoparticle networks with a mean particle size of 10–11 nm were successfully fabricated using aerosol deposition. To estimate the effects of oxygen vacancies on the optical properties of the films, UV–vis analysis was conducted as oxygen vacancies affect the optical properties of a surface forming midgap states between valence and conduction band (see Material Characterization in the Experimental Section). The absorbance spectra (Figure 2e) and the corresponding Tauc plots of as-prepared and oxygen vacant
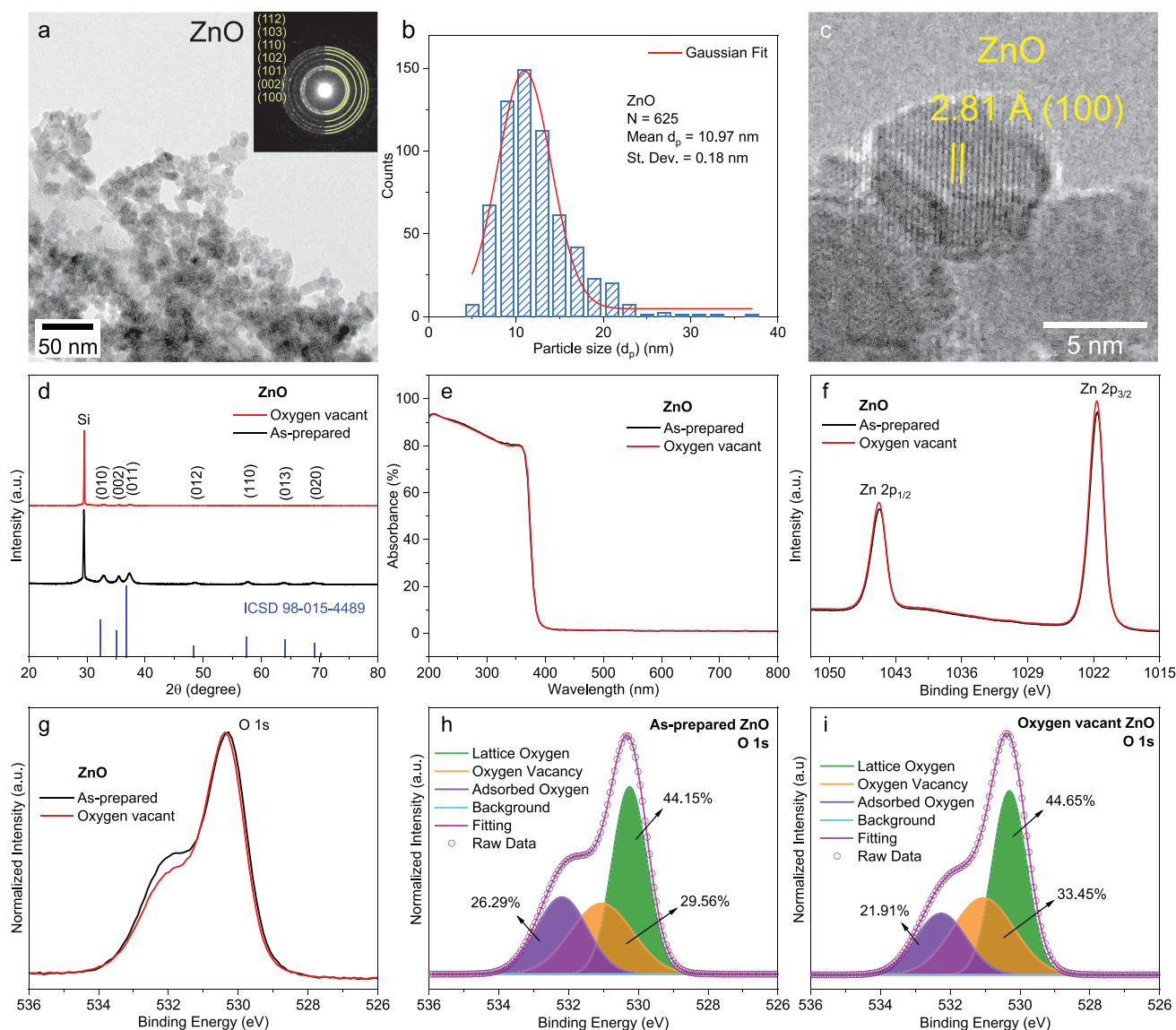
Figure 2. a) TEM image of FSP synthesized ZnO nanoparticles with the inset showing TEM diffraction pattern overlayed by the simulated pattern. b) ZnO nanoparticles analysis by TEM images. c) High-magnification TEM image of ZnO nanoparticles showing *d*-spacing of 2.81 Å corresponding to the plane (100). d) XRD patterns, e) optical absorbance, and X-ray photoelectron spectroscopy (XPS), f) high-resolution Zn 2p spectra, and g) O 1s spectra of as-prepared and oxygen vacant ZnO films. Deconvoluted O 1s peaks of h) as-prepared i) oxygen vacant ZnO films.

ZnO are presented in Figure S2b of the Supporting Information. Both as-prepared and oxygen vacant ZnO films absorb light only below 400 nm and the direct bandgap (E_g) of 3.29 eV was estimated by the Tauc plot (see Material Characterization in the Experimental Section). Both as-prepared and oxygen vacant ZnO films were optically transparent with the transmittance inversely proportional to the thickness of the film in line with our previous report.[24a] Optical analysis showed that there was no change in the optical properties of the films before and after the DUV photoactivation.

Elemental identification using high-resolution X-ray photoelectron spectroscopy (XPS) was deployed to investigate the presence of oxygen vacancies and to analyze the films before and after the DUV photoactivation. The detected elements were zinc (Zn), oxygen (O), and carbon (C) as shown in the XPS survey spectra in Figure S2c of the Supporting Information, which confirmed the high purity of fabricated ZnO films. Carbon was detected and attributed to atmospheric carbon-containing species adsorbed on the film surface during exposure to the atmosphere. All binding energies were corrected for the charge shift using the C 1s peak of graphitic carbon (binding energy = 284.6 eV) as a reference.[34] The high-resolution Zn 2p spectra showed that there was no shift in the cation binding energy after the DUV treatment (Figure 2f).

The high-resolution spectra of oxygen 1s (O 1s) showed a significant reduction in the amount of surface oxygen (Figure 2g) with a shoulder in O 1s disappearing after the DUV photoactivation. The O 1s peaks were fitted by the

ADVANCED
SCIENCE NEWS

www.advancedsciencenews.com

ADVANCED
ELECTRONIC
MATERIALS

Open Access

www.advelectronicmat.de

Gaussian–Lorentzian function, and they may be deconvoluted into three peaks, namely low, medium, and high binding energy peaks (Figure 2g–i). The deconvoluted peaks in O 1s peaks are presented in Figure 2h,i before and after the DUV photoactivation, respectively. The low binding energy peak at 530.25 eV corresponds to lattice oxygen anions (O_2^-) in the hexagonal ZnO structure (lattice oxygen peak). The medium binding energy peak at 531.05 eV has been attributed to O_x^- (O_2^- and O^-) ions in the oxygen-deficient regions due to oxygen vacancies (oxygen vacancy peak). The high binding energy peak at 532.19 eV corresponds to the loosely bound oxygen molecules at the surface or surface hydroxyl groups (adsorbed oxygen peak).[35]

After the DUV treatment, a relative decrease of 18% was observed in adsorbed oxygen species and an increase of 12% was observed in the fraction of oxygen vacancies. This is expected to improve the specific surface area and the number of reaction sites for the target gas molecules in the thick ultraporous 3D nanostructures (Figure 2h,i). A summary of XPS characteristics in O 1s spectra of as-prepared and oxygen vacant ZnO fractals is presented in Table S1 of the Supporting Information.

XPS depth profiling was carried out to estimate the distribution of oxygen vacancies in the cross-section of the thick, porous nanoparticle networks. XPS scans were recorded after every 10 s of a surface etching by Argon gas. Cross-sectional SEM analysis (Figure S3, Supporting Information) of the films at various etching times confirmed the etching rate of 0.565 nm s^{-1} for oxygen vacant ZnO porous films (see the Experimental Section).

An etching time of 2000 s removed ≈1.13 µm of the film. A thickness of 2.9 µm, more than half of the original film thickness, was removed after 5000 s of etching. **Figure 3**a shows the total atomic percentages of C 1s, O 1s, and Zn 2p as a function of ZnO film thickness. To estimate the presence and fraction of oxygen vacancies at different etching depths, the deconvolution analysis of O 1s was carried out at all depths (Figure 3a). Notably, oxygen vacancies decreased as the etching depth increased. The total amount of Zn increased and that of C decreased as the etching depth increased. However, the results suggest that the removal of atmospheric carbon molecules from the top surface does not include the removal of all oxygen-containing species such as water and hydroxyl group as the total O remains constant. The increase in Zn after the removal of the top surface is attributed to the removal of physiosorbed atmospheric compounds resulting in a higher relative fraction of Zn.

The presence of carbon at various depths was observed and attributed to the high porosity of the films as the whole film is readily exposed to the atmosphere. Deconvolution analysis of O 1s at three different depths is presented in Figure 3b–d. Oxygen vacancies were the highest (33%) at the top layer of the DUV-treated ZnO films since the top surface receives the highest intensity of DUV light. At a depth of 0.57 µm, the oxygen vacancies decreased to 27%, and the adsorbed oxygen decreased from 22% to 14%. However, at a depth of 1.13 µm, the adsorbed oxygen decreased to 13% and oxygen vacancies were 24%. This analysis shows that a significant amount of oxygen vacancies was present not only at the top layer of the films but also at an etching depth of 1.13 µm from the top surface. The relative amount of the O—Zn bond (lattice oxygen) increased as the fraction of adsorbed oxygen species decreased with increasing

depth. A summary of characteristics of deconvoluted O 1s peaks at various etching levels is presented in Table S2 of the Supporting Information.

To confirm the consistency of the XPS depth analysis and the amount of oxygen vacancies, XPS depth profiling was carried out on the same sample at two separate locations on different days. Figure 3e,f shows the O 1s spectra at two separate locations of the same sample and reveals that there was no significant difference in the intensity and the peak position of O 1s spectra at various depths. It suggests that the oxygen vacancies were distributed uniformly throughout the thick, porous films at various depths. Further depth profiling below a depth of 1.13 µm showed an increase in the amount of O and a decrease in the amount of Zn (Figure S4, Supporting Information). At an etching depth of 2.9 µm, corresponding to a remaining film thickness of 2.7 µm, the atomic percentage of Zn is less than 20% and that of O is more than 80%. This was attributed to the contribution of the oxygen in the SiO_2/Si substrate (Figure S5, Supporting Information).

Figure S6 of the Supporting Information shows a top view and cross-sectional SEM images of 0.72 and 2.13 µm thick layers at higher magnifications, demonstrating scattered ZnO fractals close to the substrate. The increase in the amount of oxygen after 1.13 µm etching was attributed to the strong signals of O_2—Si bonds from the substrate in line with the above analysis.[36] Subsequently, we conducted a detailed analysis of O 1s at increased etching depths. Figure S7a of the Supporting Information shows that the intensity of O 1s increases and the peak position shifts toward higher binding energy as the etching depth increased from 1.13 µm. The O 1s spectra at deeper levels (1.7, 2.26, and 2.82 µm etching depths) cannot be deconvoluted into more than two-component peaks as the O 1s peak shape became narrower and the component peaks converged. Due to the shift in the binding energy of O 1s spectra at higher depths, O 1s spectra were deconvoluted into two-component peaks; a low binding energy peak associated with the O—Zn bond (lattice oxygen), and a high binding energy peak associated with the O_2—Si bond. The high binding energy peaks in Figure S7b–d of the Supporting Information were not associated with adsorbed oxygen or oxygen vacancy because of the increase in the intensity of O 1s spectra, which further increased at higher depths. However, this component peak was associated with the O_2—Si bond because its intensity increased with etching depth shifting toward higher binding energy of 534 eV, associated with the O_2—Si bond in various XPS studies of silica compounds.[36,37]

The peak position of O 1s spectra at the etching depth of 2.82 µm (etching time ≈ 5000 s) was 533.5 eV. This analysis suggests that the effective photoactivation region of DUV treatment for the creation of oxygen vacancies in thick ZnO films synthesized by FSP is ≈2 µm. The reason for the drop in oxygen vacancies at increasing depths is attributed to the limited DUV penetration with increasing bulk absorption. Despite the extremely high porosity of the films, the penetration of DUV is determined by the DUV light intensity (≈30 mW cm^{-2}) and nanoparticle light absorption coefficient times their cross-sectional density.[38] UV–vis analysis of the films with various thicknesses (Figure S5, Supporting Information) was carried out and shown in Figure S8 of the Supporting Information.
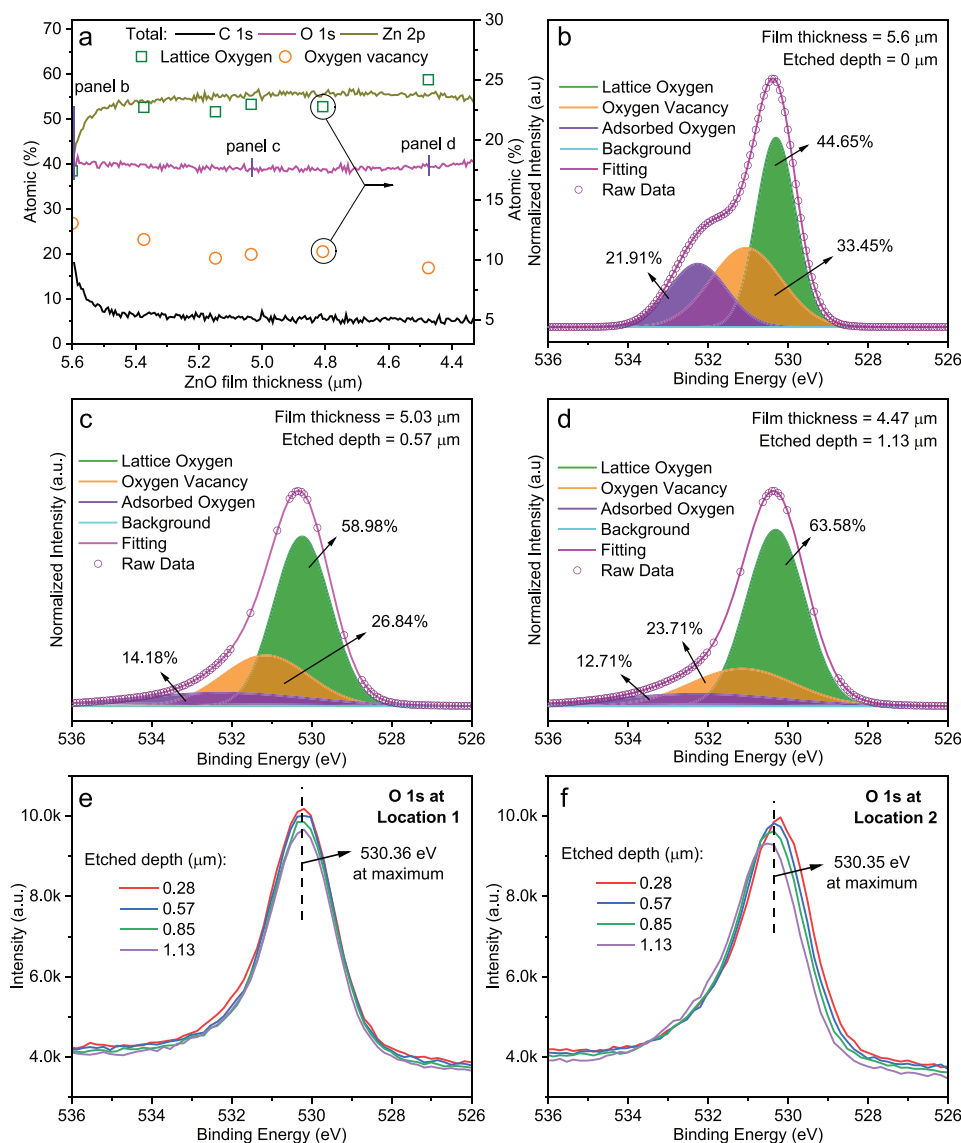
Figure 3. XPS depth analysis of oxygen vacant ZnO films at different etching depths showing a) atomic percentages of elements as a function of ZnO film thickness. The deconvoluted O 1s peaks of oxygen vacant ZnO showing oxygen vacancies at b) the top surface, c) at an etched depth of 0.57 μm, and d) at an etched depth of 1.13 μm, where the remaining ZnO film thickness is 4.47 μm. O 1s spectra at various depths obtained by XPS depth profiling at two locations e) 1, and f) 2 on the same sample geometrical area.

It shows that the transmittance decreased, and the absorbance increased as the film thickness increased. Although the films are extremely porous, the transmittance of UV light is decreased by ≈33% at a depth of 1.13 μm.

To investigate the potential of our thick ultraporous films and the role of oxygen vacancies for room temperature gas sensing, ethanol gas was used as a model analyte. The sensor response was recorded as a change in current under a constant voltage of 1 V (see the Experimental Section). All the sensors were constantly exposed to synthetic air and solar illumination (AM1.5 solar simulator, 67 mW cm^{-2}), while the exposure of the target gas was kept constant with an "in" and "out" cycle of 15 min each. The representative dynamic response curves of as-prepared ZnO for the ethanol concentration in the range of 10 ppb to 1 ppm are shown in **Figure 4**a as a function of

temperature. The response of the sensors increased with the increasing concentration of the target gas. Notably, the sensors responded to very low concentrations of ethanol and showed a higher response at lower temperatures such as 30 and 150 °C, which was attributed to the ultraporous nature of the nanostructures and the use of light irradiation. We have shown similar findings in the case of NiO–ZnO nano-heterostructures when tested in the presence of solar light.[9b] The change in the resistance of a sensor device composed of oxygen vacant ZnO in the presence of solar light is shown in Figure S9a of the Supporting Information. However, a negligible change in the current was observed for 10 and 20 ppb of ethanol at higher temperatures (Figure 4b). All sensing tests were conducted at least six times and the average responses are reported with standard errors.
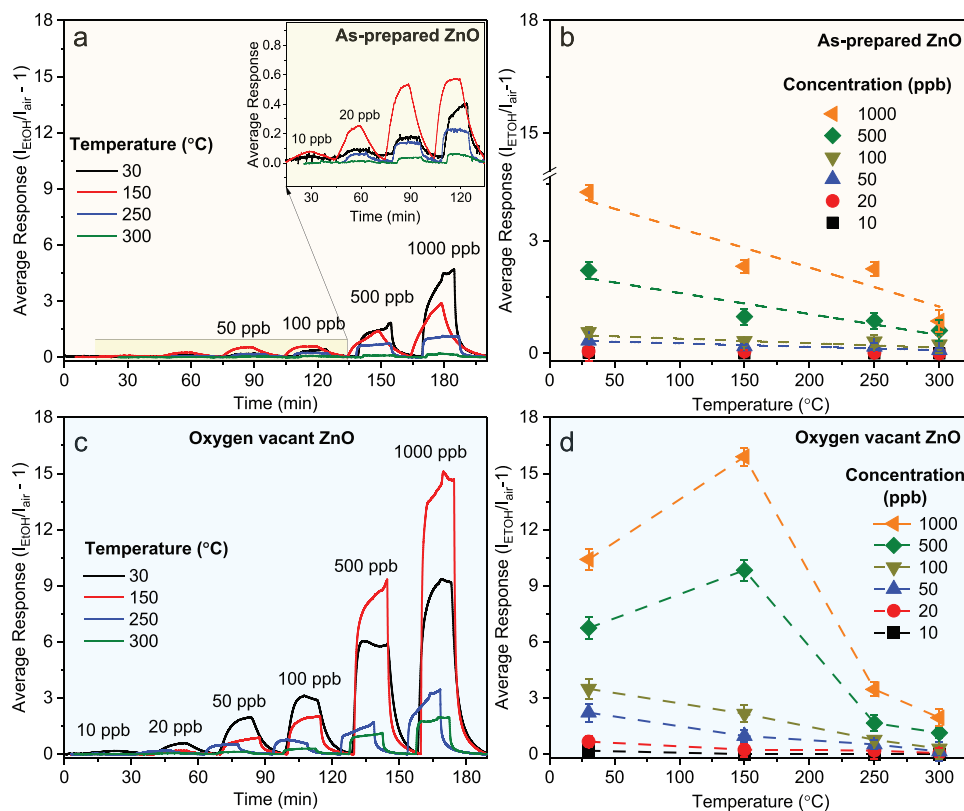
**ADVANCED
SCIENCE NEWS**

www.advancedsciencenews.com

**ADVANCED
ELECTRONIC
MATERIALS**

www.advelectronicmat.de

Figure 4. The ethanol sensing performance of as-prepared and oxygen vacant ZnO sensors. Representative dynamic response curves of a) as-prepared, and c) oxygen vacant ZnO films as a function of temperature. Average ethanol responses to different concentrations of ethanol ranging from 10 ppb to 1 ppm of b) as-prepared, d) oxygen vacant ZnO films, as a function of temperature.

The average sensor response of as-prepared ZnO increases from 0.02 to 4.3 at room temperature with increasing ethanol concentration from 10 ppb to 1 ppm (Figure 4b). This shows that even as-prepared ZnO porous films could be used for room temperature ethanol sensing under light irradiation, which was consistent with our previous work.[9b] Notably, the sensor response significantly increased at room temperature after DUV treatment as shown in Figure 4c. The DUV treatment increased the sensor response by 83% to 1 ppm of ethanol at room temperature.

Figure 4c shows the representative dynamic response curves of oxygen vacant ZnO toward ethanol as a function of temperature. The average sensor response was increased from 0.18 to 10.41 with the increasing ethanol concentration from 10 ppb to 1 ppm at room temperature, which shows an 83% increase in the response to 1 ppm of ethanol at room temperature. The maximal response of the oxygen vacant ZnO sensors was observed at 150 °C (Figure 4d). The sensor response to 1 ppm of ethanol was increased by 149% at 150 °C. The oxygen vacant ZnO sensors also showed increased response with the increasing ethanol concentration at different temperatures, with lower responses at higher temperatures. The lower responses at higher temperatures were attributed to the increased catalytic activity of the films at higher temperatures that combust ethanol molecules before reaching the most sensitive bottom part of the films near the interdigitated electrodes.

To investigate the sensitivity of the sensors for lower ppb concentrations, the response of the sensor to trace concentrations (i.e., 20 ppb of ethanol) was investigated (**Figure 5**a) as a function of temperature. Importantly, even for extremely low concentrations, the average ethanol responses of the sensors were higher at room temperature as compared to those at higher temperatures. The average response to 20 ppb of ethanol at room temperature was increased by 58% due to the presence of oxygen vacancies. Response and recovery times are important performance indicators. Oxygen vacancies also improved the average response and recovery times of the sensors at room temperature. The average response and recovery times to 20 ppb ethanol for as-prepared and oxygen vacant sensors at various temperatures are compared and presented in Table S3 of the Supporting Information. All the sensors with oxygen vacancies responded rapidly to extremely low concentrations of ethanol even at room temperature. The average response and recovery times to 20 ppb of ethanol at room temperature are compared in Figure 5b. The average response time to 20 ppb ethanol was decreased by 51% and recovery time by 64% at room temperature after the DUV treatment.

Furthermore, all the sensors showed good repeatability and stability in their sensitivity to various concentrations of ethanol at lower temperatures (Figure 5c,d). The sensor performance was analyzed for stability at room temperature and assessed with a gap of 2 weeks, however, the sensitivity of both as-prepared and oxygen vacant ZnO sensors decreased at room temperature
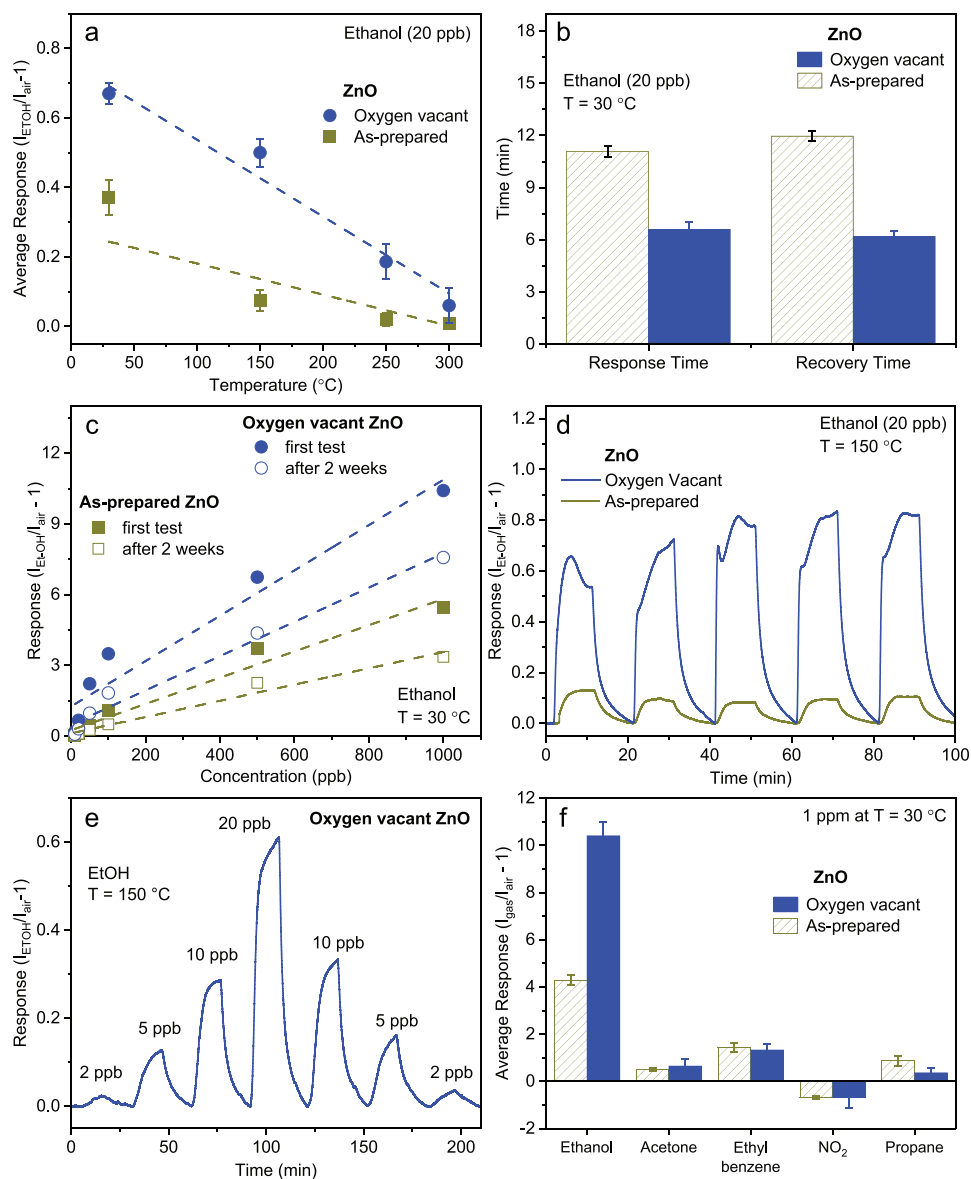
2200905 (8 of 16)

ADVANCED
SCIENCE NEWS

www.advancedsciencenews.com

ADVANCED
ELECTRONIC
MATERIALS

www.advelectronicmat.de

Figure 5. a) Average responses of as-prepared and oxygen vacant ZnO films to 20 ppb ethanol at various temperatures. b) Average response and recovery times to 20 ppb ethanol at room temperature. c) Ethanol responses after 2 weeks at room temperature. d) Consecutive 5 cycles of 20 ppb ethanol showing a stable and reproducible response of ZnO thick films at 150 °C. e) The dynamic response curve of oxygen vacant ZnO thick film to 2 to 20 ppb ethanol at 150 °C. f) The average response to 1 ppm of propane, NO$_2$, ethylbenzene, acetone, and ethanol at room temperature.

over time. To assess the long-term stability of oxygen vacant ZnO, the sensors were tested after 4 months of initial experiments at room temperature and 150 °C. A decrease of 70% and 61% was observed to 1 ppm ethanol at room temperature and 150 °C, respectively (Figure S9b, Supporting Information). Similarly, the sensors showed comparable and reproducible responses to 5 consecutive cycles of 20 ppb of ethanol at 150 °C as shown in Figure 5d. This demonstrates an excellent reproducibility and stable sensing performance to extremely low concentrations of ethanol and higher sensitivities of the oxygen vacant ZnO films than the as-prepared ZnO films. Notably, the response curves of as-prepared ZnO show saturation faster than the response of oxygen vacant ZnO to the same concentration of ethanol demonstrating the potential of higher

responses by oxygen vacant ZnO at higher temperatures and concentrations. An operating temperature of 150 °C resulted in an excellent sensitivity of oxygen vacant thick ZnO nanoparticle networks with the detection limit down to 2 ppb concentration of ethanol with repeatable responses (Figure 5e). Notably, this is the highest responsivity reported so far for ethanol sensors comprised of pure ZnO nanostructures at room temperature (see **Table 1**) and also for the presence of oxygen defects using low-temperature and low-cost DUV photoactivation treatment (see **Table 2**) among single and doped semiconductors.

Next, we investigated the selectivity of the sensors at room temperature, by exposing them to different VOCs (acetone, ethylbenzene, NO$_2$, and propane). The average responses of the as-prepared and oxygen vacant ZnO sensors are shown in

Table 1. Comparison of recent studies of room temperature VOC sensors.

Material	Temperature [°C]	External catalyst	EtOH concentration [ppm]	Responsivity [I_{EtOH}/I_{air} - 1]	Limit of detection [ppm]	Response/recovery times [s]	Refs.
Thick porous ZnO fractals	RT	Solar light	0.05	2.22	0.01	448/505	This work
			1	10.41		300/360	
ZnO–NiO nano-heterojunctions	RT	Solar light	0.1	0.77	0.01	N/A	[9b]
ZnO nanorods	RT	UV light	200	4.24[a]	N/A	52/192	[18]
Cr$_2$O$_3$-functionalized ZnO	RT	UV light	200	10.95[a]	N/A	26/110	[18]
α-Fe$_2$O$_3$/ZnO nanowires	RT	N/A	100	9.1%	100	N/A	[30a]
Au-modified ZnO nanowire	RT	N/A	20	≈10[b]	N/A	–/5	[30b]
ZnO nanodisks	RT	Thermally and UV activated	100	0.17	20	11/15	[39]
Au–ZnO nanofibers	RT	UV light	100	1.18[c]	N/A	N/A	[40]
ZnO nanotubes	RT	N/A	10	30.91[d]	N/A	263/80	[41]

[a] $I_{ethanol}/I_{air}$ *100; [b] 1-$I_{ethanol}/I_{air}$ * 100; [c] $I_{ethanol}/I_{air}$; [d] 1-$I_{air}/I_{ethanol}$ * 100.

Figure 5f. It was observed that the oxygen vacancies significantly improved the selectivity of ZnO films toward ethanol. The selectivity of oxygen vacant ZnO films, at room temperature, was increased 20-fold as compared to other VOCs. The lower responses of other VOCs at room temperature were associated with the difference in the polarity of VOC molecules. Generally, ethanol molecule shows higher binding affinities and the bipolar hydroxyl group (OH) in ethanol molecule interacts with the surface via two different charge transfer mechanisms as compared to monopolar molecules such as acetone. This has been reported recently for room temperature sensing of SnO$_2$ as well and confirmed, both experimentally and theoretically.[42] Furthermore, the ethanol testing was carried out with oxygen vacant ZnO sensors in realistic conditions for the possible application as breath analyzers in relative humidity of 30%, 50%, and 80% at room temperature. The sensors showed a rapid response to the higher concentrations of ethanol (100–1000 ppb) as shown in Figure S9d of the Supporting Information, however, the responses were lower in humid conditions as compared to the dry conditions. This was attributed to the lower number of reaction sites available to the ethanol in the presence of an interfering gas such as H$_2$O molecules as well as the low operating temperature of the sensors.

This was also in agreement with the DFT results of our as-prepared and oxygen vacant ZnO nanostructures presented in

Table 2. Comparison of recently developed ethanol sensors with oxygen defects.

Material	Sensing temperature [°C]	Oxygen vacancy introduction process	EtOH concentration [ppm]	Responsivity [I_{EtOH}/I_{air} - 1]	Limit of detection [ppm]	Response/recovery times [s]	Refs.
Thick porous ZnO fractals	RT	DUV photoactivation at 200 °C	0.05	2.22	0.01	448/505	This work
			1	10.41		300/360	
Thick porous ZnO fractals	150	DUV photoactivation at 200 °C	0.05	0.97	0.005	371/486	This work
			1	15.9		260/312	
ZnO nanorod arrays	400	H$_2$O$_2$ thermal treatment at 400 °C	3	≈70[a]	1	N/A	[35a]
Rutile SnO$_2$ nanostructures	190	Reduction by NaBH$_4$	20	37.2[a]	N/A	42/17	[43]
SnO$_2$ nanocolumns	RT	Reducing environment (argon)	400	1.27	N/A	N/A	[42]
In$_2$O$_3$ octahedral particles	200	Phase transformation process from In(OH)$_3$ at 300 °C	1000	610[a]	N/A	1–2/15–20	[15]
ZnO nanosheets	330	Preferential [0001] growth direction at 500 °C	50	80[a]	N/A	N/A	[44]
Co-doped ZnO microspheres	220	Co doping at 400 °C	5	3.3[a]	N/A	N/A	[45]
Ce-doped ZnO nanostructures	300	Ce-doping at 450 °C	100	72.6[a]	N/A	9/3	[46]
ZnO/SnO$_2$ composite hollow spheres	225	Hydrothermal process, calcination at 400 °C	30	34.8[a]	0.5	1/–	[47]

[a] $I_{ethanol}/I_{air}$.

ADVANCED
SCIENCE NEWS
www.advancedsciencenews.com

ADVANCED
ELECTRONIC
MATERIALS
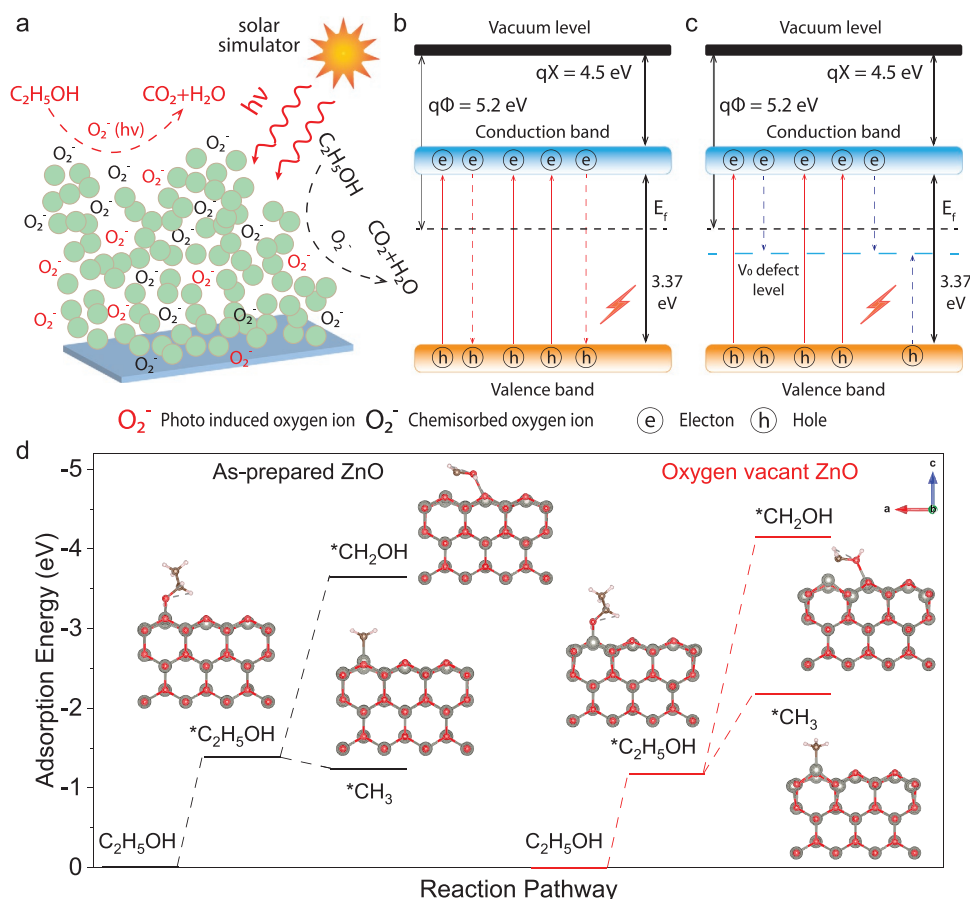Open Access
www.advelectronicmat.de

Figure 6. A schematic illustration of a) chemisorption of oxygen molecules on nanoparticles and ethanol sensing mechanism of ultraporous ZnO nanoparticle networks under solar irradiation. Energy band structure of b) as-prepared ZnO, and c) oxygen vacant ZnO d) calculated geometric configurations and corresponding adsorption energies of C_2H_5OH, CH_3, and CH_2OH on as-prepared and oxygen vacant ZnO.

Figure S11 of the Supporting Information. The adsorption energies of acetone, ethylbenzene, propane, and NO_2 were found to be lower than that of ethanol in the case of both as-prepared and oxygen vacant ZnO surfaces. The adsorption energies calculated by DFT for all VOCs have been summarized in Table S4 of the Supporting Information. The response of an oxidizing gas, NO_2, was observed in the reverse order as compared to other VOCs, confirming electrons were the majority charge carrier in ZnO films, a typical response shown by n-type semiconductors. The interaction of an oxidizing gas, such as NO_2, with an n-type semiconductor, such as ZnO, causes an increase in the resistance of the semiconductor as opposed to other VOCs, which cause a decrease in the resistance of an n-type semiconductor. Importantly, this negative response can also be used for the selective detection of this important analyte at room temperature for breath analysis.

The excellent performance of the oxygen vacant ZnO films as gas sensors at room temperature has been attributed to (a) the presence of oxygen vacancies in the ultraporous morphology, (b) photocatalytic oxidation of ethanol under solar irradiation, and (c) the unique 3D ultraporous morphology of ZnO films with electron-depleted domains. A possible sensing mechanism was related to the adsorption and desorption of molecules on the ZnO surface; under ambient conditions,

oxygen molecules adsorb on the surface of ZnO and create a depletion region by trapping electrons from the surface and forming chemisorbed oxygen species (O_2^-, O^-) (see **Figure 6**a). Oxygen vacancies act as electron donors and enable the formation of more chemisorbed oxygen species on the surface and thus provide more reaction sites for the target gas molecules. The chemisorbed oxygen species (O_2^-, O^-) are thermally stable at lower temperatures and cannot desorb from the surface of ZnO.[48] Under solar irradiation, photon absorption occurs and the generated photoelectrons react with chemisorbed oxygen species and form photoinduced oxygen ions

$$O_2 + e^- \xrightarrow{h\nu} O_2^- (h\nu) \tag{2}$$

and the surface electron/hole centers Zn^+ and O^- are generated in pair

$$Zn^+ - O_2^- \xrightarrow{h\nu} Zn^+ - O^- \tag{3}$$

These photoinduced oxygen ions have more reactivity as compared to chemisorbed oxygen ions and are weakly bound to the ZnO surface.[49] $Zn^+ - O^-$ centers also serve as the active sites for ethanol molecules activation and their oxidation. Furthermore, the oxygen vacancies also promote charge

**ADVANCED
SCIENCE NEWS**
www.advancedsciencenews.com

**ADVANCED
ELECTRONIC
MATERIALS**
www.advelectronicmat.de

separation and prolong the life of photoinduced charge carriers leading to effective generation and stability of active electron–hole centers.[21] To explore the physical phenomenon of oxygen vacancies modulating the sensing performances, the schematics of carrier excitation and recombination are illustrated in Figure 6b,c. Oxygen vacancies in semiconductors are generally considered deep-level defects located at energy levels lower than the conduction band.[50] Oxygen vacancies act as charge killers and trap the excited electrons, in addition to the chemisorbed oxygen, inducing a further decrease in effective charge carriers as shown in Figure 6c. Whereas, oxygen vacancies lower the band gap of the metal oxide, increase the electrons in the conduction band as shown in Figure 6c, and therefore, enable effective electron transport during the sensing reaction and hence improve the sensitivity at lower temperatures.

Upon exposure to a target gas, such as ethanol, the photoinduced oxygen ions, and chemisorbed oxygen ions participate in the redox reactions at room temperature and electrons are released by the oxidation of ethanol.

$$C_2H_5OH + 3O_2^-(h\nu) \rightarrow 2CO_2 + 3H_2O + 3e^- \qquad (4)$$
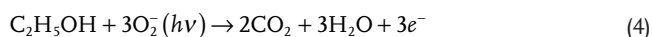
Oxygen vacancies would promote the ethanol activation process by promoting the chemisorption and photoadsorption of oxygen molecules and increasing the electron densities. Thus, oxygen vacancies increase the concentration of highly reactive sites and the adsorption energy of the target gas molecule for chemical sensing. As a result, while both as-prepared and oxygen vacant ZnO nanostructures were activated by light illumination, oxygen vacant ZnO nanostructures have significantly higher chemical sensing responses.

In addition, the ultraporous and 3D network of ZnO nanoparticles facilitates the presence of oxygen vacancies in the whole film as opposed to the dense films where only surface oxygen vacancies are created and take part in the redox reaction process. This morphology also promotes the deep reversible penetration of target gas molecules into the films allowing the whole film to participate in the gas sensing process, in line with our previous work, demonstrating faster adsorption and desorption of molecules and deep penetration of light in ultraporous nanoparticle networks for high-performance UV photodetectors.[24a] The high specific surface area of these ultraporous nanostructures provides many readily available sites for catalytic activity and thus increases the sensitivity of the films. This unique morphology and low probability of electron–hole recombination due to the oxygen vacancies are mainly responsible for the fast response and recovery times of oxygen vacant ZnO films.

Lower responses of the films, particularly, oxygen vacant ZnO films to ethanol, at higher temperatures were associated with decreasing concentration of oxygen vacancies and combustion of ethanol molecules at higher temperatures. At higher temperatures, oxygen defects become mobile and the high-energy O atoms diffuse into the lattice structure and become the lattice O atoms by occupying the oxygen vacancies (V_O), hence, decreasing the concentration of oxygen vacancies. The formation of lattice oxygen by oxidization to form ideally stoichiometric ZnO at higher temperatures is represented as

$$ZnO : V_O^+ + e^- + 1/2O_2 \rightarrow ZnO \qquad (5)$$

To gain a mechanistic understanding of the relationship of oxygen vacancies to ethanol sensing performances, DFT calculations were conducted with a ZnO slab with and without oxygen vacancies (see the Experimental Section). The models of as-prepared and oxygen vacant ZnO $(10\bar{1}0)$ slabs are shown in Figure S10 of the Supporting Information. The adsorption energies of ethanol on ZnO were calculated and are presented in Figure 6d with the corresponding geometric configurations. The results show that the oxygen vacancies increase the ethanol adsorption energy as compared to the ethanol adsorption energy on the surface of as-prepared ZnO. Ethanol molecules adsorb on the ZnO surface and dissociate into intermediate components. There are various routes for ethanol disassociation on the surface of MOS films and the associated charge carrier migration is quite intricate.[51] However, in our case, it suggested that oxygen vacancies favor the breaking of the C−C bond of ethanol and thus increase the adsorption of ethanol. The ethanol molecule can dissociate into CH_3 and CH_2OH on the surface of ZnO, before complete oxidation into H_2O and CO_2, due to the presence of oxygen vacancies and the use of solar irradiation, which lowers the energy barrier required to break the C−C bond.[52] The ethanol disassociation reaction was summarized by

$$CH_3CH_2OH_{(ads)} \rightarrow CH_{3(ads)} + CH_2OH_{(ads)} \qquad (6)$$
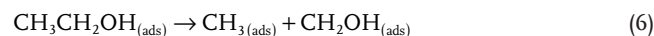
In the case of as-prepared ZnO, the adsorption energies are lower for CH_3 and CH_2OH, which shows that disassociation of ethanol was not favorable, and ethanol adsorb loosely on the surface of as-prepared ZnO films. Whereas, in the presence of oxygen vacancies, the adsorption energies increase, showing that the oxygen vacancies favor the disassociation of ethanol molecules and increase the adsorption of its products on the surface of the oxygen vacant ZnO films. Our combined theoretical and experimental results reveal that the oxygen vacancies in thick, ultraporous ZnO nanoparticle networks promote the catalytic activity of ZnO by generating Zn^+/O^- pairs, which act as active centers for the dissociation of ethanol and thus promote the adsorption of ethanol at room temperature which results in enhanced sensitivity and selectivity.

3. Conclusions

Here, we introduce the engineering of highly sensitive low-temperature semiconductor chemical sensors, consisting of thick networks of oxygen vacant ZnO nanoparticles, via a facile and scalable two-step process. For the first time, we demonstrate that, in these ZnO nanoparticle networks, a gentle low-temperature DUV treatment can induce up to 24% of oxygen vacancies down to a depth of 1.13 µm, allowing to tune the surface properties throughout their cross-section. This is attributed to the high porosity of the networks that results in a high UV light penetration and an accessible nanoparticle surface. We also demonstrated by XPS depth profiling that variable and consistent amount of oxygen vacancies can be generated by adjusting the film thickness, the light intensity, and wavelength. The optimal oxygen-vacant films demonstrated a significantly improved low-temperature chemical sensing performance with

sensitivity to 1 ppm ethanol increasing by 83% at room temperature to 149% at 150 °C and response and recovery times to 20-ppb ethanol decreasing by 51% and 64%, respectively, at room temperature. At 150 °C, these sensors achieved a record low detection limit of 2 ppb of ethanol. Their performance was also characterized by a panel of other gas molecules such as acetone, ethylbenzene, propane, and NO_2, revealing that the oxygen vacancies preserve the characteristic ZnO n-type semiconductor behavior. To understand the improvement in the sensing performance, a DFT analysis of the interaction of these gas molecules with the oxygen vacant and stoichiometric ZnO surfaces was performed. It was observed that oxygen vacancies promote the adsorption and dissociation of ethanol, lowering the activation energy for its reaction on the oxygen vacant ZnO surface. We believe that these insights on the structural–functional correlation of oxygen vacant ZnO nanoparticle networks and the facile and scalable fabrication process provide a path for the engineering of low-power yet extremely sensitive miniaturized devices for wearable and distributed chemical sensor networks, with a potential contribution to the internet of things and massive sensor arrays. Furthermore, the facile tuning of the photocatalytic activity and surface band structure of these ZnO nanoparticle networks is of interest for a variety of photocatalytic processes and optoelectronic applications.

4. Experimental Section

Materials: All materials were used as received without any further purification. Zinc naphthenate (10% Zn, Merck) was used as a precursor and dissolved in xylene (Merck) to generate a solution with a total Zn metal atom concentration of 0.3 м. The solution was stirred for 30 min at room temperature to ensure complete dispersion.

Fabrication of ZnO: An FSP was used to synthesize, and for direct deposition of ZnO nanoparticles on Pt interdigitated electrodes.[11a,53] The Zn precursor solution was delivered via an automatic syringe pump (New Era syringe pump; Model: NE-300) at a flow rate of 5 mL min⁻¹ and dispersed into a fine spray with 7 L min⁻¹ oxygen at a constant pressure drop of 2 bars. The spray was ignited by supporting premixed methane/oxygen flames (CH_4 = 1.2 L min⁻¹, O_2 = 2 L min⁻¹). Glass substrates containing 180 pairs of Pt interdigitated electrodes of 5 µm width and spacing (Micrux, Spain) were placed on a water-cooled substrate holder at a height above burner of 20 cm. All substrates were cleaned three times with ethanol before deposition. After FSP deposition, the substrates were heat-treated at 300 °C for 12 h in a furnace (Brother High-Temperature Furnace XD-1.2KN) to stabilize the nanoparticle size and avoid resistive sintering during the gas sensing measurements. For the DUV photoactivated modulation of FSP-ZnO films, a customized temperature-controllable system was adopted for precise temperature control, and a home-made DUV irradiation system was designed by using an excimer lamp (UV emission wavelength of 172 nm, 20×12 cm², Wonik Q & C) with the constant intensity of UV ≈ 30 mW cm⁻². Dry N_2 gas was supplied to the customized chamber to prevent the formation of ozone (O_3) and the FSP-ZnO films and sensor devices were identically heated at 200 °C for 2 h under DUV.

Material Characterization: Topographical and optical characterization techniques were used to analyze the morphology of the samples. Analytical scanning electron microscopy (Zeiss Ultra Plus field emission scanning electron microscope) was used for morphological analysis at 3 kV. The results were analyzed using ImageJ software and the FracLac plugin. Information about the morphology, particle size, and lattice plane spacing was acquired using a high-resolution transmission electron microscope (JEOL 2100F HRTEM) operated at 200 kV. A small amount of powder sample was added to ethanol and sonicated for

20 min to achieve a stable suspension, followed by casting a drop onto Lacey carbon 200 mesh Nickel grids. The particle size distribution was evaluated by manually measuring the size of 625 nanoparticles using ImageJ. The simulation of the polycrystalline TEM diffraction patterns was performed using the JEMS[54] code as implemented on version 4.6131U2018. A Bruker D2 Phaser diffractometer was utilized to perform XRD). Each sample was scanned using a Cu Kα (1.54 Å) radiation source with an operating voltage of 30 kV and a current of 10 mA. The XRD patterns were recorded with a scan rate of 0.75° min⁻¹ in the 2θ range of 10°–80° at an increment of 0.02°. The modified Scherrer equation[33] was applied to accurately calculate the crystalline domain size. XRD patterns were analyzed by commercially available software, HighScore Plus using the database of ICSD. Modified Scherrer equation was used to accurately estimate the size of nanoparticles from XRD peaks[33] and was given by

$$\ln \beta = \ln \frac{1}{\cos \theta} + \ln \frac{K\lambda}{D} \tag{7}$$

where β was the full width at half maximum, in radians, located at any 2θ position in the pattern, λ (nm) was the radiation of wavelength, K was the Scherrer constant or shape factor, and D was the particle size in nm.

UV–vis transmittance and absorption spectra were measured using a PerkinElmer (Lambda 1050 UV/vis/NIR) spectrophotometer. The characterization for both atomic orbital and chemical composition was analyzed by XPS (K-APLPHA+, Thermo Fisher Scientific) using a monochromated Al-Kα source. Further depth profiling was carried out through a repetitive process of Ar etching for 10 s and an immediate XPS scan. The ultraporous ZnO films were deposited on SiO_2/Si substrates for SEM, XRD, and XPS analysis while on quartz substrates for UV–vis analysis. For absorbance measurements, quartz substrates of fused silica were used. All the measurements were taken in the presence of ambient air and the absorbance/transmittance of ZnO films were compared with blank quartz substrate.

The optical transmittance and reflectance of light were measured using UV–vis analysis. The data are presented in percentages to show the percentage of light transmitted or reflected through a film/sample. Based on the transmittance and reflectance data obtained, the following equation was used to calculate the absorbance of a film Absorbance = 100 – transmittance – reflectance.

The Tauc plot was used to compute the optical bandgap of semiconductors using Tauc and Davis–Mott relation from UV–vis absorption spectroscopy

$$(\alpha h v)^n = K \left(h v - E_g \right) \tag{8}$$

In this relation, α is the absorption coefficient, hv is incident photon energy, K is energy independent constant, and E_g is the optical bandgap energy. While the exponent, n, represents the nature of transition and its value is 2 for indirect bandgap and ½ for direct bandgap materials.[55]

Max Plank equation was used to calculate energy from wavelength using

$$E_g = h v \tag{9}$$

where h is Plank's constant and v is the frequency of the incident photon.

Also

$$v = \frac{c}{\lambda} \tag{10}$$

where c is the speed of light and λ is the wavelength of the incident photon.

From Equations (9) and (10), the following equation is obtained

$$E_g = \frac{hc}{\lambda} \tag{11}$$

**ADVANCED
SCIENCE NEWS**

www.advancedsciencenews.com

**ADVANCED
ELECTRONIC
MATERIALS**

www.advelectronicmat.de

After inserting the values and converting them to joules, the following equation is obtained

$$E_g = \frac{1240 \text{ eV nm}}{\lambda} \tag{12}$$

The absorption coefficient, α, was calculated from the absorbance data using Beer–Lambart law.[56] The equation after rearranging and inserting the values is given below

$$\alpha = 2.303 \left(\frac{A}{L}\right) \tag{13}$$

where A is the absorbance and L is the light's path length where the absorbance takes place. The unit of absorption coefficient is cm^{-1} as the absorbance is dimensionless.

AXS measurements were performed at the SAXS/WAXS beamline of the Australian Synchrotron in Melbourne, Australia in transmission mode with a photon energy of 12 keV and a sample to detector length of $\approx$7.2 m. The images were recorded using a 2D Pilatus 2 M hybrid pixel detector using exposure times between 0.5 and 5 s. Accurate calibration of the q range was done for each group of measurements using a Silver Behenate (AgBeh) standard.

The porosity, ε, was estimated from gravimetric and cross-sectional SEM analysis as previously suggested[13b]

$$\varepsilon = 1 - \frac{T_{bulk}}{T_{SEM}} \tag{14}$$

where T_{SEM} was the thickness of the ZnO fractals measured from cross-sectional SEM, while T_{bulk} was the equivalent bulk thickness given by

$$T_{bulk} = \frac{V_{ZnO}}{A} = \frac{m}{\rho_{ZnO}A} \tag{15}$$

here, m was the mass of deposited material onto the substrate of area A and ρ was the average density of the fractal media.

Sensing Measurements: The sensing measurements were performed as follows: VOCs (ethanol, 9.91 ppm in N_2 (Coregas); acetone, 10.1 ppm in N_2 (Coregas); ethylbenzene, 10 ppm in N_2 (BOC Ltd); and propane, 10 ppm in N_2 (BOC Ltd)) were controlled by a mass flow controller (Bronkhorst) and further diluted with simulated air (0.1 L min^{-1} O_2 + 0.4 L min^{-1} N_2 (BOC Ltd.)) to reach the desired concentration (from 2 ppb to 1 ppm) and the total gas flow rate was still kept at 0.5 L min^{-1}. The temperature of a stage in the sensing chamber (Linkam) was controlled by a temperature controller and the sample was illuminated through a quartz window by a solar simulator (NewSpec, LCS-100) with an AM1.5 filter glass. The dynamic response of the gas sensor was recorded by an electrochemical workstation (CHI 660E, USA) under a constant applied voltage of 1 V. Standard errors were calculated in the sensing measurements by performing sensing experiments at least three times with the same experimental conditions and the average responses are presented as the sensor response. The sensing response of the sensors was calculated as

$$\text{Sensor response} = \left(\frac{I_{gas}}{I_{air}}\right) - 1 \tag{16}$$

where I_{gas} was the current in the presence of target gas and I_{air} was the current in the air without the target gas. The target gas flowed into the sensing chamber for 15 min and was then switched off for 15 min. The response and recovery times were calculated using a threshold of 90% change in the response in the presence and absence of the target gas, respectively.

DFT Calculations: The DFT calculations were implemented using the Vienna ab-initio simulation package with the core and valence electronic interactions modeled using the projector augmented wave method. The Perdew–Burke–Ernzerhof exchange-correlation functional was employed. The wavefunctions were expanded with a kinetic energy cut-off of 500 eV, and a Monkhorst–Pack k-points of $7 \times 7 \times 1$ was used. Geometrical optimizations were achieved by relaxing all ionic positions and supercell vectors until the Hellmann–Feynman forces were less than 0.01 eV Å^{-1}. A vacuum region of 20 Å was introduced in the direction of the z-axis to avoid interactions between periodic images. The dispersion correction was performed in this study using the DFT-D3 method. The adsorption energies (E_{ads}) were computed using the following equation

$$E_{ads} = E_{(ZnO + adsorbates)} - E_{(ZnO)} - E_{(adsorbates)} \tag{17}$$

The Monkhorst–Pack k-points of $13 \times 13 \times 1$ were used for the density of states calculation.

Supporting Information

Supporting Information is available from the Wiley Online Library or from the author.

Acknowledgements

Conflict of Interest

The authors declare no conflict of interest.

Data Availability Statement

The data that support the findings of this study are available from the corresponding author upon reasonable request.

[1] a) D. Marazziti, P. Cianconi, F. Mucci, L. Foresi, I. Chiarantini, A. D. Vecchia, *Sci. Total Environ.* **2021**, *773*, 145182; b) C. Martinez-Perez, C. Alvarez-Peregrina, C. Villa-Collar, M. A. Sanchez-Tena, *Int. J. Environ. Res. Public Health* **2020**, *17*, 7690.

[2] a) J. Wood, World Economic Forum, Geneva, Switzerland, Vol. *2022*, **2022**; b) Y. Zhu, J. Xie, F. Huang, L. Cao, *Sci. Total Environ.* **2020**, *727*, 138704; c) M. Petroni, D. Hill, L. Younes, L. Barkman, S. Howard, I. B. Howell, J. Mirowsky, M. B. Collins, *Environ. Res. Lett.* **2020**, *15*, 0940a9.

[3] a) T. Lin, X. Lv, Z. Hu, A. Xu, C. Feng, *Sensors* **2019**, *19*, 233; b) A. T. John, K. Murugappan, D. R. Nisbet, A. Tricoli, *Sensors* **2021**, *21*, 2271.

[4] a) A. Chizhov, M. Rumyantseva, A. Gaskov, *Nanomaterials* **2021**, *11*, 892; b) W. Ding, D. Liu, J. Liu, J. Zhang, *Chin. J. Chem.* **2020**, *38*, 1832.

[5] F. Bovey, J. Cros, B. Tuzson, K. Seyssel, P. Schneiter, L. Emmenegger, L. Tappy, *Nutr. Diabetes* **2018**, *8*, 50.

[6] E. Kabir, N. Raza, V. Kumar, J. Singh, Y. F. Tsang, D. K. Lim, J. E. Szulejko, K. H. Kim, *Chem* **2019**, *5*, 3020.

[7] A. Tricoli, M. Righettoni, A. Teleki, *Angew. Chem., Int. Ed. Engl.* **2010**, *7632*, 7632.

[8] a) A. Marikutsa, M. Rumyantseva, E. A. Konstantinova, A. Gaskov, *Sensors* **2021**, *21*, 2554; b) V. Gurylev, T. P. Perng, *J. Eur. Ceram. Soc.* **2021**, *4977*, 4977.

[9] a) J. Wang, H. C. Shen, Y. Xia, S. Komarneni, *Ceram. Int.* **2021**, *47*, 7353; b) H. Chen, R. Bo, A. Shrestha, B. Xin, N. Nasiri, J. Zhou, I. Di Bernardo, A. Dodd, M. Saunders, J. Lipton-Duffin, T. White, T. Tsuzuki, A. Tricoli, *Adv. Opt. Mater.* **2018**, *6*, 1800677.

[10] a) H. X. Yu, C. Y. Guo, X. F. Zhang, Y. M. Xu, X. L. Cheng, S. Gao, L. H. Huo, *Adv. Sustainable Syst.* **2022**, *6*, 2100370; b) S. M. Majhi, A. Mirzaei, H. W. Kim, S. S. Kim, T. W. Kim, *Nano Energy* **2021**, *79*, 105369; c) Y. Chen, M. Li, W. Yan, X. Zhuang, K. W. Ng, X. Cheng, *ACS Omega* **2021**, *6*, 1216.

[11] a) R. Bo, F. Zhang, S. Bu, N. Nasiri, I. Di Bernardo, T. Tran-Phu, A. Shrestha, H. Chen, M. Taheri, S. Qi, Y. Zhang, H. K. Mulmudi, J. Lipton-Duffin, E. D. Gaspera, A. Tricoli, *ACS Appl. Mater. Interfaces* **2020**, *12*, 9589; b) E. Pargoletti, U. H. Hossain, I. Di Bernardo, H. Chen, T. Tran-Phu, J. Lipton-Duffin, G. Cappelletti, A. Tricoli, *Nanoscale* **2019**, *11*, 22932.

[12] a) A. T. John, K. Murugappan, M. Taheri, D. R. Nisbet, A. Tricoli, *J. Mater. Chem. C* **2021**, *9*, 17331; b) Z. U. Abideen, J.-H. Kim, S. S. Kim, *Sens. Actuators, B* **2017**, *238*, 374.

[13] a) Z. Fusco, M. Rahmani, R. Bo, R. Verre, N. Motta, M. Kall, D. Neshev, A. Tricoli, *Adv. Mater.* **2018**, *30*, 1800931; b) Z. Fusco, M. Rahmani, T. Tran-Phu, C. Ricci, A. Kiy, P. Kluth, E. D. Gaspera, N. Motta, D. Neshev, A. Tricoli, *Adv. Mater.* **2020**, *32*, 2002471.

[14] a) M. Righettoni, A. Tricoli, S. Gass, A. Schmid, A. Amann, S. E. Pratsinis, *Anal. Chim. Acta* **2012**, *738*, 69; b) M. Righettoni, A. Tricoli, S. E. Pratsinis, *Anal. Chem.* **2010**, *82*, 3581.

[15] J. J. Liu, G. Chen, Y. G. Yu, Y. L. Wu, M. J. Zhou, H. Q. Zhang, C. D. Lv, Y. Zheng, F. He, *RSC Adv.* **2015**, *5*, 44306.

[16] Q. A. Drmosh, Y. A. Al Wajih, I. O. Alade, A. K. Mohamedkhair, M. Qamar, A. S. Hakeem, Z. H. Yamani, *Sens. Actuators, B* **2021**, *338*, 129851.

[17] L. X. Cai, G. Y. Miao, G. Li, L. Chen, F. L. Meng, Z. Guo, *IEEE Sens. J.* **2021**, *21*, 25590.

[18] S. Park, G. J. Sun, C. Jin, H. W. Kim, S. Lee, C. Lee, *ACS Appl. Mater. Interfaces* **2016**, *8*, 2805.

[19] a) N. Joshi, T. Hayasaka, Y. Liu, H. Liu, O. N. OliveiraJr., L. Lin, *Microchim. Acta* **2018**, *185*, 213; b) D. Degler, U. Weimar, N. Barsan, *ACS Sens.* **2019**, *4*, 2228; c) L. Zhu, W. Zeng, *Sens. Actuators, A* **2017**, *267*, 242.

[20] a) M. Al-Hashem, S. Akbar, P. Morris, *Sens. Actuators, B* **2019**, *301*, 126845; b) J. Wang, R. S. Chen, L. Xiang, S. Komarneni, *Ceram. Int.* **2018**, *44*, 7357.

[21] J. Wang, C. Y. Hu, Y. Xia, B. Zhang, *Sens. Actuators, B* **2021**, *333*, 129547.

[22] K. Haddad, A. Abokifa, S. Kavadiya, B. Lee, S. Banerjee, B. Raman, P. Banerjee, C. Lo, J. Fortner, P. Biswas, *ACS Appl. Mater. Interfaces* **2018**, *10*, 29972.

[23] H. Yuan, S. Aljneibi, J. Yuan, Y. Wang, H. Liu, J. Fang, C. Tang, X. Yan, H. Cai, Y. Gu, S. J. Pennycook, J. Tao, D. Zhao, *Adv. Mater.* **2019**, *31*, 1807161.

[24] a) N. Nasiri, R. Bo, F. Wang, L. Fu, A. Tricoli, *Adv. Mater.* **2015**, *27*, 4336; b) N. Nasiri, R. Bo, L. Fu, A. Tricoli, *Nanoscale* **2017**, *9*, 2059.

[25] W.-J. Lee, J.-G. Choi, S. Sung, C.-H. Kim, S. Na, Y.-C. Joo, S. Park, M.-H. Yoon, *ACS Appl. Mater. Interfaces* **2021**, *13*, 2820.

[26] a) S. W. Fan, A. K. Srivastava, V. P. Dravid, *Appl. Phys. Lett.* **2009**, *95*, 142106; b) A. Tricoli, M. Graf, F. Mayer, S. Kuhne, A. Hierlemann, S. E. Pratsinis, *Adv. Mater.* **2008**, *20*, 3005; c) Z. Fusco, T. Tran-Phu, A. Cembran, A. Kiy, P. Kluth, D. Nisbet, A. Tricoli, *Adv. Photonics Res.* **2021**, *2*, 2100020.

[27] T. Tran-Phu, R. Daiyan, Z. Fusco, Z. Ma, R. Amal, A. Tricoli, *Adv. Funct. Mater.* **2019**, *30*, 1906478.

[28] a) B. Fazio, P. Artoni, M. A. Iati, C. D'Andrea, M. J. Lo Faro, S. Del Sorbo, S. Pirotta, P. G. Gucciardi, P. Musumeci, C. S. Vasi, R. Saija, M. Galli, F. Priolo, A. Irrera, *Light: Sci. Appl.* **2016**, *5*, 16062; b) G. C. Bushell, Y. D. Yan, D. Woodfield, J. Raper, R. Amal, *Adv. Colloid Interface Sci.* **2002**, *95*, 1.

[29] T. Tran-Phu, R. Daiyan, J. Leverett, Z. Fusco, A. Tadich, I. Di Bernardo, A. Kiy, T. N. Truong, Q. Zhang, H. Chen, P. Kluth, R. Amal, A. Tricoli, *Chem. Eng. J.* **2022**, *429*, 132180.

[30] a) D. Zhu, Y. Fu, W. Zang, Y. Zhao, L. Xing, X. Xue, *Mater. Lett.* **2016**, *166*, 288; b) A. L. Zou, Y. Qiu, J. J. Yu, B. Yin, G. Y. Cao, H. Q. Zhang, L. Z. Hu, *Sens. Actuators, B* **2016**, *227*, 65.

[31] a) R. E. Plotnick, R. H. Gardner, W. W. Hargrove, K. Prestegaard, M. Perlmutter, *Phys. Rev. E* **1996**, *53*, 5461; b) E. Fernandez, H. F. Jelinek, *Methods* **2001**, *24*, 309.

[32] S. Mishra, E. Przezdziecka, W. Wozniak, A. Adhikari, R. Jakiela, W. Paszkowicz, A. Sulich, M. Ozga, K. Kopalko, E. Guziewicz, *Materials* **2021**, *14*, 4048.

[33] A. Monshi, M. R. Foroughi, M. R. Monshi, *World J. Nano Sci. Eng.* **2012**, *02*, 154.

[34] a) C. D. Wagner, L. H. Gale, R. H. Raymond, *Anal. Chem.* **2002**, *51*, 466; b) R. Al-Gaashani, S. Radiman, A. R. Daud, N. Tabet, Y. Al-Douri, *Ceram. Int.* **2013**, *39*, 2283.

[35] a) W. Kim, M. Choi, K. Yong, *Sens. Actuators, B* **2015**, *209*, 989; b) Y. Tu, S. Q. Chen, X. Li, J. Gorbaciova, W. P. Gillin, S. Krause, J. Briscoe, *J. Mater. Chem. C* **2018**, *6*, 1815.

[36] a) A. Hashemi, A. Bahari, *Appl. Phys. A: Mater. Sci. Process.* **2017**, *123*, 535; b) M. Copuroglu, H. Sezen, R. L. Opila, S. Suzer, *ACS Appl. Mater. Interfaces* **2013**, *5*, 5875.

[37] Y. Hijikata, H. Yaguchi, M. Yoshikawa, S. Yoshida, *Appl. Surf. Sci.* **2001**, *184*, 161.

[38] H. Palneedi, J. H. Park, D. Maurya, M. Peddigari, G. T. Hwang, V. Annapureddy, J. W. Kim, J. J. Choi, B. D. Hahn, S. Priya, K. J. Lee, J. Ryu, *Adv. Mater.* **2018**, *30*, 1705148.

[39] M. R. Alenezi, A. S. Alshammari, K. D. Jayawardena, M. J. Beliatis, S. J. Henley, S. R. Silva, *J. Phys. Chem. C* **2013**, *117*, 17850.

**ADVANCED
SCIENCE NEWS**

www.advancedsciencenews.com

**ADVANCED
ELECTRONIC
MATERIALS**

www.advelectronicmat.de

[40] E. Wongrat, N. Chanlek, C. Chueaiarrom, B. Samransuksamer, N. Hongsith, S. Choopun, *Sens. Actuators, A* **2016**, *188*, 188.

[41] D. Acharyya, P. Bhattacharyya, *Sens. Actuators, B* **2016**, *228*, 373.

[42] A. A. Abokifa, K. Haddad, J. Fortner, C. S. Lo, P. Biswas, *J. Mater. Chem. A* **2018**, *6*, 2053.

[43] Q. H. Zeng, Y. F. Cui, L. F. Zhu, Y. W. Yao, *Mater. Sci. Semicond. Process.* **2020**, *111*, 104962.

[44] J. Q. Xu, Z. G. Xue, N. Qin, Z. X. Cheng, Q. Xiang, *Sens. Actuators, B* **2017**, *148*, 148.

[45] J. J. Xu, S. J. Li, L. Li, L. Y. Chen, Y. F. Zhu, *Ceram. Int.* **2018**, *44*, 16773.

[46] Y. Q. Zhang, Y. Y. Liu, L. S. Zhou, D. Y. Liu, F. M. Liu, F. M. Liu, X. S. Liang, X. Yan, Y. Gao, G. Y. Lu, *Sens. Actuators, B* **2018**, *273*, 991.

[47] J. Y. Liu, T. S. Wang, B. Q. Wang, P. Sun, Q. Y. Yang, X. S. Liang, H. W. Song, G. Y. Lu, *Sens. Actuators, B* **2017**, *551*, 551.

[48] Y. C. Xu, H. Z. Li, B. J. Sun, P. Z. Qiao, L. P. Ren, G. H. Tian, B. J. Jiang, K. Pan, W. Zhou, *Chem. Eng. J.* **2020**, *379*, 122295.

[49] F. Liu, X. Wang, X. Chen, X. Song, J. Tian, H. Cui, *ACS Appl. Mater. Interfaces* **2019**, *11*, 24757.

[50] a) A. Kabir, I. Bouanane, D. Boulainine, S. Zerkout, G. Schmerber, B. Boudjema, *Silicon* **2018**, *11*, 837; b) F. Yang, J. M. Guo, L. Zhao, W. Y. Shang, Y. Y. Gao, S. Zhang, G. Q. Gu, B. Zhang, P. Cui, G. Cheng, Z. L. Du, *Nano Energy* **2020**, *67*, 104210; c) S. Li, J. Yue, X. Ji, C. Lu, Z. Yan, P. Li, D. Guo, Z. Wu, W. Tang, *J. Mater. Chem. C* **2021**, *9*, 5437.

[51] a) C. Y. Xie, Y. L. Sun, B. Z. Zhu, P. Guo, J. Z. Liu, *J. Mater. Sci.* **2021**, *56*, 17096; b) T. Yang, Y. Liu, W. Jin, Y. Han, S. Yang, W. Chen, *ACS Sens.* **2017**, *2*, 1051.

[52] S. Satyapal, J. Park, R. Bersohn, B. Katz, *J. Chem. Phys.* **1989**, *91*, 6873.

[53] T. Tran-Phu, R. Daiyan, X. M. C. Ta, R. Amal, A. Tricoli, *Adv. Funct. Mater.* **2021**, *32*, 2110020.

[54] P. A. Stadelmann, *Ultramicroscopy* **1987**, *21*, 131.

[55] a) P. Makula, M. Pacia, W. Macyk, *J. Phys. Chem. Lett.* **2018**, *9*, 6814; b) B. D. Viezbicke, S. Patel, B. E. Davis, D. P. Birnie, *Phys. Status Solidi B* **2015**, *252*, 1700.

[56] a) D. F. Swinehart, *J. Chem. Educ.* **1962**, *39*, 333; b) T. G. Mayerhofer, A. V. Pipa, J. Popp, *ChemPhysChem* **2019**, *20*, 2748.